

# APPLICATION OF DEEP LEARNING FOR ACOUSTIC IMPEDANCE ANALYSIS AND PERFORMANCE PREDICTION IN A FREE-PISTON STIRLING ENGINE

Wenlian YE<sup>1,2,\*</sup>, Haiyang LONG<sup>1</sup>, Weijie WANG<sup>1</sup>, Lulu HU<sup>3</sup>, Yingwen LIU<sup>4</sup>

<sup>1</sup>Key Laboratory of Advanced Pumps Valves and Fluid Control System, Ministry of Education,

College of Energy and Power Engineering, Lanzhou University of Technology, Lanzhou, Gansu, 730050 PR China

<sup>2</sup>Zhe Jiang AMA&HIEN Technology Co., Ltd., Yueqing, Zhejiang, 325600 PR China

<sup>3</sup>School of Mechanical Engineering, Jiangsu University of Technology, Changzhou, Jiangsu, 213100 PR China

<sup>4</sup>Key Laboratory of Thermo-Fluid Science and Engineering of MOE, School of Energy and Power Engineering, Xi'an Jiaotong University, Xi'an, Shaanxi 710049 PR China

Corresponding author; E-mail: ywl-315@lut.edu.cn

*A coupled thermodynamic-dynamic model of a  $\gamma$ -type free-piston Stirling engine is developed using Sage software to analyze impedance characteristics and predict output performance by applying two neural network algorithms. The model accounts for four key thermodynamic and dynamic parameters. These parameters determine acoustic impedance, output power, and efficiency. The results show that as a charge pressure is 2.0MPa, increasing the porosity from 0.86 to 0.93 leads to output power and efficiency increased from 22.17W to 35.12 W and the efficiency increased from 18.44% to 23.26%. At a charge pressure of 2.5MPa, as the spring stiffness of the piston rises from  $1.0 \times 10^4 \text{N/m}$  to  $1.7 \times 10^4 \text{N/m}$ , the real part of the acoustic impedance increases from  $3.374 \times 10^7 \text{Pa}\cdot\text{s/m}$  to  $3.384 \times 10^7 \text{Pa}\cdot\text{s/m}$  and the virtual part of the acoustic impedance decreases from  $1.343 \times 10^7 \text{Pa}\cdot\text{s/m}$  to  $1.320 \times 10^7 \text{Pa}\cdot\text{s/m}$ . Furthermore, the study employs a CNN algorithm to predict efficiency and output power, comparing its performance with that of an ANN algorithm. The CNN model demonstrates exceptional predictive accuracy, achieving an  $R^2$  value above 0.99 and a mean squared error below 2. This study demonstrates the effectiveness of integrating deep learning with simulation-based modeling to enable rapid and accurate performance prediction, offering a scalable approach for the design optimization of FPSE systems in energy applications.*

*Keywords: Free-piston Stirling engine; Performance analysis; Convolutional neural network; Acoustic impedance*

## 1. Introduction

The rapid advancement of space technology, coupled with the escalating demands of deep space exploration missions, necessitates the development of more sophisticated and

high-performance space power supply systems. The free-piston Stirling generator (FPSG), functioning as an advanced thermal-to-electrical, can be applied as a continuous power source for space power generation owing to its unique characteristics, including high efficiency of thermoelectric conversion, low noise, high reliability, and long life[1]. The FPSG consists of a free-piston Stirling engine (FPSE) and a linear generator. The FPSE was developed by Dr. Beale in 1964[2] and received a lot of attention from countries all over the world. The FPSE can not only use various heat sources such as solar energy, nuclear energy[3], biomass energy, and radioisotope energy but also demonstrates exceptional capability in harnessing low-grade thermal energy sources, including industrial waste heat. Generally, the kinematic Stirling engines consist of three types:  $\alpha$ -type,  $\beta$ -type, and  $\gamma$ -type[4], and since the piston and displacer of the  $\gamma$ -type FPSE are arranged in parallel, it has the advantage of simple structure. So the  $\gamma$ -type FPSE is applied in this paper.

In recent years, researchers have focused on the analyses of the thermodynamic, dynamic, thermodynamic-dynamic, and performance optimization of the FPSE. Li et al.[5] analyzed the the performance of FPSE by building a corresponding analysis code, to couple the thermodynamic cycle analysis model with the mechanical motion model of the piston and the linear alternator characteristic model. Zare et al.[6]conducted an analytical investigation into FPSEs, introducing a novel approach based on practical stability theory and dynamic error analysis. Notably, considering vanishing disturbances and comparing the motions of the two pistons, alongside identifying limit cycles, led to a more accurate estimation of the damping coefficient range. In addition, they introduced the concept of the “ultimate bound” as a quantitative metric to evaluate design accuracy. The methodology shows its effectiveness in enhancing the predictability and performance of FPSE systems. Tavakolpour et al.[7] proposed an averaging-based Lyapunov method to systematically analyze the thermodynamic instability of FPSEs and explore the conditions for the existence of limit cycles. This method not only deepens the understanding of the working mechanism of FPSEs, but also provides an effective tool for its performance prediction and optimization design. Wu et al.[8] proposed a quasi-static one-dimensional numerical model with a linear generator with sensitivity analysis and a semi-implicit discretization algorithm of the FPSE. The predicted values of the output parameters of the system were similar with the design values under stable operating conditions, and the relative error between the expected and actual values of the output power was 2.66%. The accuracy of the model and the higher prediction accuracy of the FPSE output parameters were verified. Ahmadi et al.[9] propose a method for predicting the output power of a solar Stirling heat engine, which is optimized through a hybrid approach combining Genetic Algorithm (GA) and Particle Swarm Optimization (PSO). This approach enhances the prediction accuracy by leveraging the strengths of both GA and PSO for optimization, enabling the neural network to better model the complex relationship between engine parameters and power output. The proposed model demonstrates improved performance in forecasting power, offering a more reliable tool for solar Stirling engine design and operation. Tavakolpour et al.[10] presents a multi-objective optimization of a Stirling heat engine using the Grey Wolf Optimizer (GWO). The algorithm effectively enhances thermal efficiency and output power by optimizing key engine parameters. The results reveal that GWO outperforms conventional algorithms in terms of convergence speed and solution accuracy.

While existing research on FPSE mainly focuses on performance analysis and thermodynamic coupling, challenges remain in coupling coordination due to mechanical parameter mismatches between the Stirling engine and the linear alternator. This study introduces the concept of impedance to analyze load characteristics and optimize parameter matching. Meanwhile, with the rapid advancement of artificial intelligence and deep learning techniques, researchers have increasingly adopted data-driven methods in combination with multi-objective optimization frameworks to address complex challenges involving high-dimensional and nonlinear datasets. Classical optimization algorithms, such as GA, PSO, and the GWO, have been widely used for optimizing the design and performance of free-piston Stirling engines and thermal-acoustic systems[9-10]. While these methods provide flexibility in handling nonlinear, multi-objective problems, they typically depend on accurate mathematical modeling and require extensive simulations to achieve convergence. Their performance is also highly sensitive to parameter tuning and often lacks scalability in large-scale design spaces. To address the limitations above, we propose a deep learning-based method utilizing Convolutional Neural Networks (CNN). The CNNs have gained widespread adoption due to their high computational efficiency, reduced reliance on manual feature engineering, and superior predictive performance on large-scale datasets[11]. Once trained, The CNN can swiftly predict output power and efficiency across various design parameters, eliminating the need for repeated, computationally intensive thermodynamic simulations. This significantly reduces the computational burden of parametric analyses and facilitates real-time performance evaluation. While CNNs are predominantly applied in fields such as image recognition, visual analytics[12], and remote sensing prediction[13], their use in forecasting the output power and thermal efficiency of FPSE systems remains largely unexplored. Furthermore, a direct comparative analysis between CNN-based models and conventional Artificial Neural Networks (ANN) in this specific application has yet to be thoroughly investigated.

This study develops a thermodynamic-dynamic coupled model in Sage software to analyze the impact of four key input parameters on FPSE performance. Analyzing the change of these output parameters across extensive value ranges significantly increases the computational demand. To overcome this limitation, we proposed and implemented an advanced CNN model trained on simulation data to accurately predict the performance characteristics of the FPSE. This machine learning-based strategy effectively reduces the need for exhaustive numerical simulations, enhances prediction precision, and improves the overall efficiency of parametric studies. Simultaneously, the performance of the CNN algorithm and ANN algorithm in predicting output power and efficiency is systematically compared. The strengths and weaknesses of the two algorithms are thoroughly evaluated in terms of prediction accuracy, based on performance metrics such as  $R^2$  and MSE. The findings of this study provide a valuable theoretical foundation and technical support for the optimization and design of FPSE systems.

## **2. Model description**

### **2.1 System introduction**

Fig. 1 illustrates the schematic configuration of a  $\gamma$ -type free-piston Stirling generator, which consists of two primary subsystems: the FPSE and the linear generator. The FPSE subsystem incorporates three distinct working spaces (expansion, compression, and buffer spaces) and four key components: a heater, a regenerator, a cooler, and two moving elements (displacer and piston). The piston and displacer are mechanically supported by individual plate springs, which provide essential axial stiffness while maintaining the required freedom of movement in response to pressure differentials.

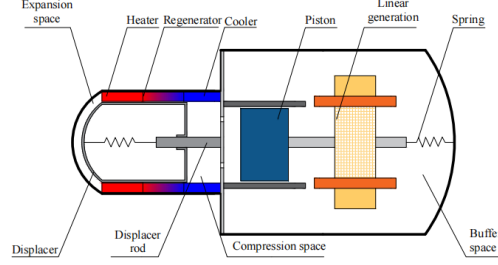


**Fig. 1 Schematic of  $\gamma$ -type FPSE with external load**

As shown in Fig. 1, according to Newton's second law, the equilibrium relationship between the displacer and the piston is given by[3]:

$$m_d \ddot{x}_d + c_d \dot{x}_d + k_d x_d = A_d (p_c - p_e) - A_{rd} (p_c - p_b) \quad (1)$$

$$m_p \ddot{x}_p + c_p \dot{x}_p + k_p x_p = -A_p (p_c - p_b) - F_{load} \quad (2)$$

where  $A_d$ ,  $A_p$ ,  $A_{rd}$  denote the area of the displacer, piston, and displacer rod, respectively;  $c_d$  and  $c_p$  are the damping coefficients of the displacer and piston;  $F_{load}$  represents the instantaneous electromagnetic damping force on the piston, i.e. the resistance generated by the external load attached to the piston;  $m_d$  and  $m_p$  are the masses of the displacer and piston;  $k_d$  and  $k_p$  are the spring stiffness of the displacer and piston;  $p_b$ ,  $p_c$ ,  $p_e$  are the pressure of the buffer, compression, and expansion spaces, respectively;  $x_d$  and  $x_p$  represent the displacement of the displacer and the piston;  $\dot{x}_d$  and  $\dot{x}_p$  represent the velocity of the displacer and the piston;  $\ddot{x}_d$  and  $\ddot{x}_p$  represent the accelerations of the displacer and the piston.

## 2.2 Sage model

Based on the schematic of  $\gamma$ -type FPSE in Fig.1, a thermodynamic-dynamic coupled model is built by the Sage software. The Sage software, developed by David Gedeon in 1995 using MS-DOS[14], is a quasi-one-dimensional numerical computation tool for alternating flow. It is mainly used for the design and optimization of Stirling engines[15]. The Sage software employs a modular approach to model the various components of the FPSE, with Each module encapsulating the corresponding mathematical and physical equations, as well as empirical formulas derived from extensive experiments[16]. These modules offer components such as heat and pressure sources, heat exchangers, working spaces, etc. The appropriate interfaces are selected to connect the modules and complete the modeling process[17].

The state parameters for the entire region are determined by solving the continuity,

momentum, and energy equations for each node within the nodal region, as follows[18]:

$$\frac{\partial \rho A}{\partial t} + \frac{\partial \rho u A}{\partial x} = 0 \quad (3)$$

$$\frac{\partial \rho A}{\partial t} + \frac{\partial u \rho u A}{\partial x} + \frac{\partial p}{\partial x} A - FA = 0 \quad (4)$$

$$\frac{\partial \rho e A}{\partial t} + p \frac{\partial A}{\partial t} + \frac{\partial}{\partial x} (u \rho e A + u p A + q) - Q_w = 0 \quad (5)$$

where  $A$  indicates the cross-sectional area of the gas flow path;  $e$  denotes the mass energy;  $\rho$  denotes the density of the working gas;  $u$  indicates the fluid flow rate;  $F$  represents the viscous pressure gradient in the Stokes stress tensor[18].

$$F = -\frac{\rho u |u|}{2} \left( \frac{f}{d_h} + \frac{K}{L} \right) \quad (6)$$

In this paper, the regenerator is of a random fiber matrix. The screen friction factor of the regenerator and Nusselt number for heat transfer between the regenerator and working gas is expressed as follows[18]:

$$f = \frac{\alpha_1}{\text{Re}} + \alpha_2 \text{Re}^{\alpha_3} \quad (7)$$

$$\text{Nu} = 1 + 0.186 \alpha P e^{0.55} \quad (8)$$

$$\alpha_1 = 25.7 \alpha + 79.8$$

$$\alpha_2 = 0.146 \alpha + 3.76$$

$$\alpha_3 = -0.00283 \alpha - 0.0748$$

$$\alpha = \frac{\beta}{1 - \beta}$$

The heater and cooler adopt a fin heat exchanger. The screen friction factor of the heater and cooler are as follows:

$$f = 0.11 \left( \frac{\varepsilon}{d_h} + \frac{68}{\text{Re}} \right)^{0.25} \quad (9)$$

where  $\beta$  indicates the regenerators' porosity;  $\varepsilon$  is the average height of the surface irregularity.

In the energy equation, the heat exchange per unit length, donated as  $Q_w$ , between the working gas and the wall is produced by the heat transfer from the thin film flow of the gas along the wall, and it is expressed as follows:

$$Q_w = \text{Nu} \frac{k_{gas}}{d_h} A_x (T_w - T) \quad (10)$$

where  $k_{gas}$  denotes the thermal conductivity of the working gas;  $A_x$  represents the cross-sectional area per unit length of the gas region;  $T_w - T$  denotes the temperature difference between fluid passing through the surface and the average cross-section area.

Fig. 2 shows the Sage model diagram. The above equations are embedded into the

program as constraints of Sage, and appropriate components are selected for modeling. Meanwhile, by adjusting the different input parameters, each output parameter required by the FPSE system can be derived, including acoustic impedance, output power, and thermal-to-power efficiency.

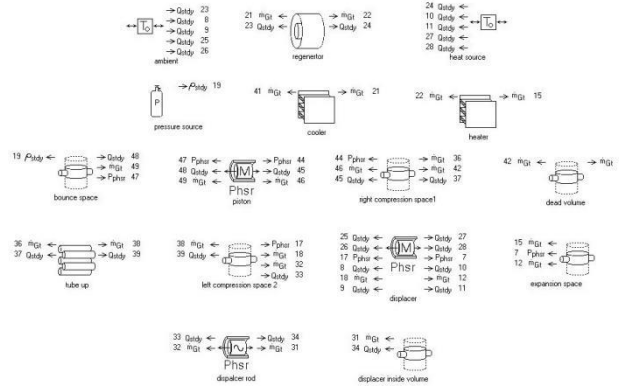


**Fig. 2** The Sage model of the  $\gamma$ -type FPSE

### 2.3 Description of the acoustic impedance

As the core component of the FPSG system, the linear alternator undertakes the key task of converting thermal energy into electrical energy. Impedance, as a key system parameter, can reflect the energy transfer efficiency between the linear alternator and the FPSE. Through impedance analysis, the energy loss problem caused by mechanical parameter mismatch can be solved, thereby improving the output power and overall performance. At the same time, since the impedance characteristics directly affect the efficiency, adjusting the impedance can effectively optimize the integrated design of the engine and the linear alternator.

The piston transfers the acoustic power from the engine to the alternator. According to the thermo-acoustic principle, the acoustic impedance  $Z_p$  of the piston is defined as[19]:

$$Z_p = \frac{P_p}{U_p} \quad (11)$$

where  $P_p$  is the pressure wave in the compression space in the FPSE,  $U_p$  denotes the volumetric flow of the gas through the piston.

In the Sage software,  $P_p$  and  $U_p$  are represented as follows:

$$P_p = p_{\cos} + ip_{\sin} \quad (12)$$

$$U_p = \frac{Mdot_{\cos} + iMdot_{\sin}}{\rho A_p} \quad (13)$$

where  $p_{\cos}$  and  $p_{\sin}$  denote the cosine and sine coefficients of the first harmonic of the pressure Fourier series;  $Mdot_{\cos}$  and  $Mdot_{\sin}$  are the cosine and sine coefficients of the first harmonic of the Fourier series of the mass flow rate at the negative boundary; and  $\rho$  is the density of the working gas.

The output electric power  $W_e$  of the alternator is expressed as[20]:

$$W_e = \frac{1}{2} R_{er} I_a^2 \quad (14)$$

where  $I_a$  denotes the current amplitude, and  $R_{er}$  denotes the external resistance.

The linear alternator efficiency, i.e. acoustic-electric efficiency is expressed as:

$$\eta_{Fe} = \frac{W_e}{W_F} \quad (15)$$

where  $W_F$  denotes the acoustic power.

### 3. Deep neural networks

To predict the performance of FPSE more accurately and efficiently, this paper adopts Matlab software and compares the results of the CNN algorithm to predict the output power and thermal-to-electric efficiency with the ANN algorithm. Through this comparative analysis, the advantages and disadvantages of the two algorithms are more comprehensively compared, thus providing a more reliable method for predicting FPSE performance.

The ANN algorithm is a computational paradigm comprising numerous interconnected processing units called neurons. The input layer, serving as the network's interface, contains a predefined number of neurons corresponding to the dimensionality of the input features. The hidden layer, which forms the core computational component of the network, performs crucial transformations through weighted connections and bias terms. The output layer should ideally hold an equal number of neurons as required and provide the final output[21]. As a multi-layer feed-forward neural network model in deep learning, CNN can extract spatial connectivity information between layers from data and represent internally relevant features. The CNN algorithm includes convolutional layers for feature extraction, pooling layers for dimensionality reduction, and fully connected layers for classification. A distinctive characteristic of CNN's network architecture lies in its utilization of specialized convolution kernels at each layer, enabling the systematic extraction of discriminative features from localized regions within the input data space. Therefore, CNN is widely used for large amounts of data processing and accurate prediction and analysis of data with good generalization ability. The steps of the CNN model used to predict the dynamic performance of the FPSE are shown in Fig. 3.

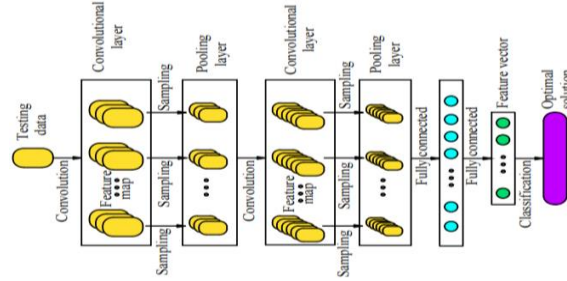


**Fig. 3 The flow diagram of CNN**

For the performance evaluation of the training and testing models in CNN and ANN, performance evaluation indicators are completed by the coefficient of multiple determinations ( $R^2$ ), Mean-Squared Error (MSE), and Root Mean Square Error (RMSE). The above parameters are specified as follows:

$$R^2 = 1 - \frac{\sum_{i=1}^M (t_{1i} - t_{2i})^2}{\sum_{i=1}^M t_{1i}^2} \quad (16)$$

$$RMSE = \sqrt{\frac{1}{M} \sum_{i=1}^M (t_{1i} - t_{2i})^2} \quad (17)$$

$$MSE = \frac{1}{M} \sum_{i=1}^M (t_{1i} - t_{2i})^2 \quad (18)$$

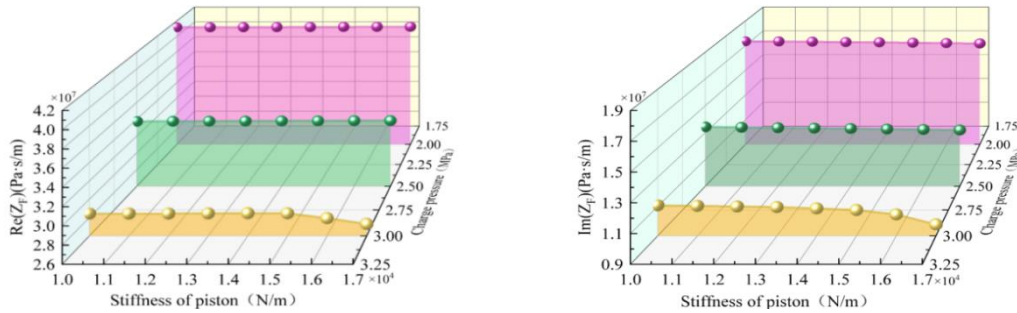
where  $M$  is the number of data;  $t_{1i}$  and  $t_{2i}$  are the experimental and predicted values, respectively. Typically,  $R^2 \in [0,1]$ , when  $R^2$  is close to 1, it indicates a better prediction of the model and a better fit to the data; when  $R^2$  is close to 0, it indicates a poor fit to the model.

## 4. Results and discussion

### 4.1 Analysis of the effects of parameters on the FPSE's performance

#### 4.1.1 Effect of the piston spring stiffness

The variation of FPSE acoustic impedance with piston spring stiffness at different charge pressures is illustrated in Fig. 4. At a charge pressure of 2.5MPa, as the piston spring stiffness increases, the real part of the acoustic impedance increases from  $3.374 \times 10^7 \text{Pa} \cdot \text{s/m}$  to  $3.384 \times 10^7 \text{Pa} \cdot \text{s/m}$ . At a charge pressure of 3.0MPa, the real and virtual parts of the acoustic impedance exhibit a gradual decrease with increasing piston spring stiffness. When the spring stiffness is below  $1.5 \times 10^4 \text{N/m}$ , the real part remains nearly constant while the virtual part decreases slightly.

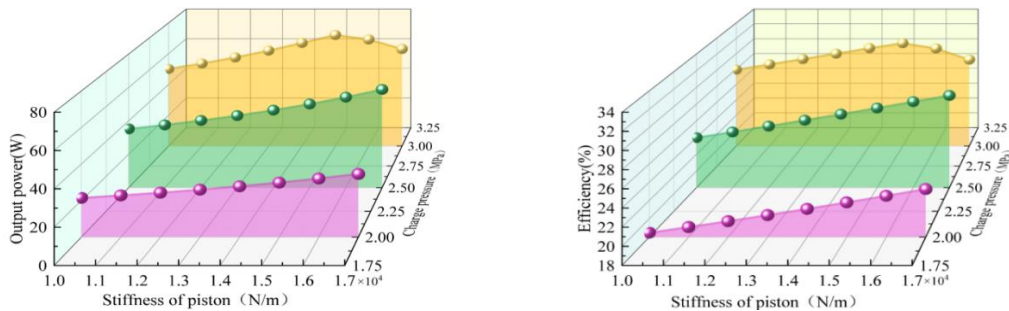


(a) The real part of acoustic impedance

(b) The virtual part of acoustic impedance

**Fig. 4** Effects of charge pressure and stiffness of piston on the acoustic impedance

The acoustic impedance of the FPSE as a function of piston spring stiffness at different charge pressures is shown in Fig. 5. At a charge pressure of 2.5MPa, increasing the spring stiffness of the piston leads to an increase in output power from 35.19 W to 64.04 W and an improvement in efficiency from 23.99% to 29.79%. At a charge pressure of 3.0MPa, both the output power and efficiency of the FPSE showed a tendency to increase and then decrease with the increase of the spring stiffness of the piston.



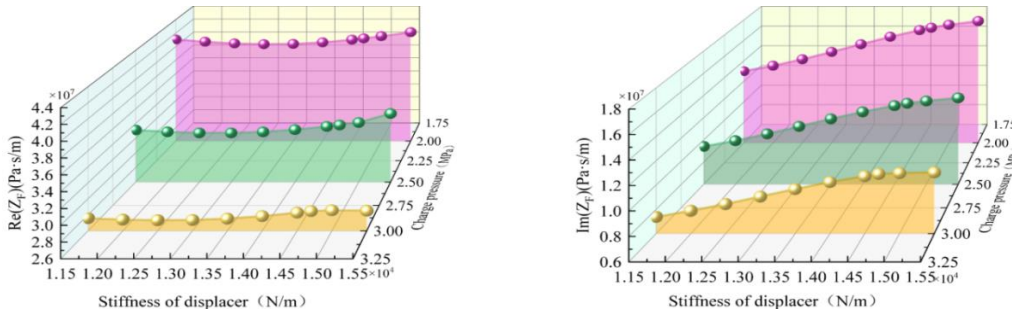
(a) Output power

(b) Efficiency

**Fig. 5** Effects of charge pressure and stiffness of piston on the performance

#### 4.1.2 Effect of the displacer spring stiffness

Fig. 6 represents the variation of Stirling engine acoustic impedance with the spring stiffness of the displacer at different charge pressure conditions. As can be seen in Fig. 6(a), the real part of acoustic impedance shows a tendency to increase and then decrease with the increase of the spring stiffness of the displacer when the charge pressure is 2.0MPa, 2.5MPa, and 3.0MPa. As shown in Fig. 6(b), the virtual part of acoustic impedance increases as the spring stiffness of the displacer increases, and the growth rate decreases gradually. At a charge pressure of 3.0MPa, increasing the spring stiffness of the displacer from  $1.15 \times 10^4 \text{N/m}$  to  $1.55 \times 10^4 \text{N/m}$  leads to an increase in the virtual part of acoustic impedance from  $7.379 \times 10^6 \text{Pa} \cdot \text{s/m}^3$  to  $1.105 \times 10^7 \text{Pa} \cdot \text{s/m}^3$ .

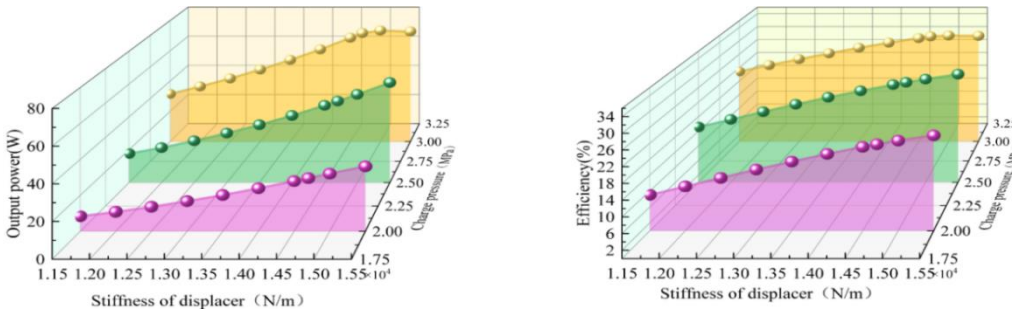


(a) The real part of acoustic impedance

(b) The virtual part of acoustic impedance

**Fig. 6** Effects of charge pressure and stiffness of displacer on the acoustic impedance

The acoustic impedance of FPSE with the spring stiffness of the displacer at different charge pressures is shown in Fig. 7. Both the output power and efficiency increased linearly with the increase of the spring stiffness of the displacer at the charge pressures of 2.0MPa and 2.5MPa. At a charge pressure of 2.5MPa, increasing the spring stiffness of the displacer from  $1.15 \times 10^4 \text{N/m}$  to  $1.55 \times 10^4 \text{N/m}$  leads to an increase in output power from 17.71W to 60.99W, and an improvement in efficiency increased from 15.24% to 29.71%.



(a) Output power

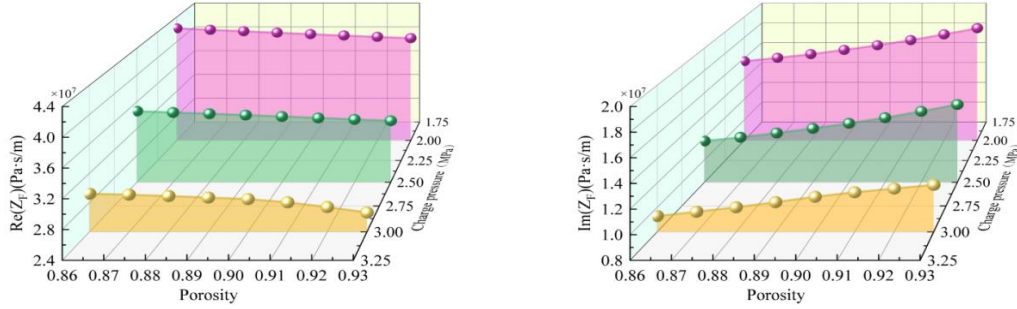
(b) Efficiency

**Fig. 7** Effects of charge pressure and stiffness of displacer on the performance

#### 4.1.3 Effect of the porosity

The variation curves of acoustic impedance with the regenerators' porosity for FPSE at different charge pressures are shown in Fig. 8. As shown in the figure, the real part of acoustic

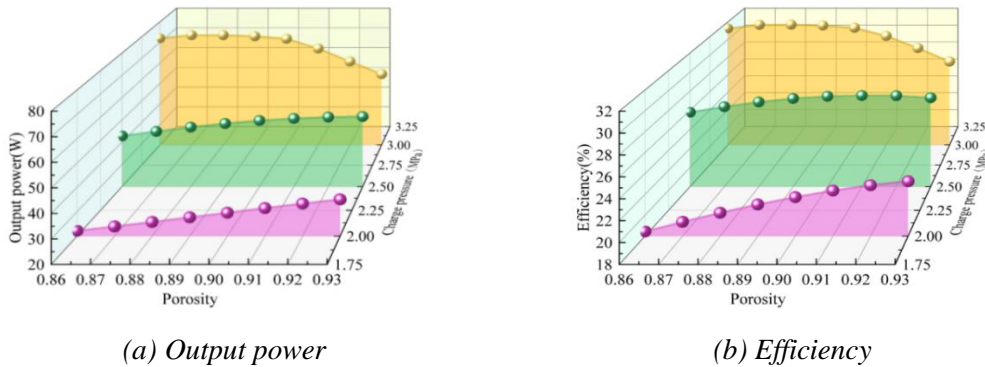
impedance decreases with the increase of porosity, and the virtual part of acoustic impedance increases with the increase of porosity under different charge pressure conditions. When the charge pressure is 3.0MPa, the porosity increases from 0.86 to 0.93, the real part of acoustic impedance decreases from  $2.920 \times 10^7 \text{Pa}\cdot\text{s}/\text{m}$  to  $2.666 \times 10^7 \text{Pa}\cdot\text{s}/\text{m}$ , and the virtual part of acoustic impedance increases from  $9.294 \times 10^6 \text{Pa}\cdot\text{s}/\text{m}$  to  $1.186 \times 10^7 \text{Pa}\cdot\text{s}/\text{m}$ .



(a) The real part of acoustic impedance      (b) The virtual part of acoustic impedance

**Fig. 8 Effects of charge pressure and porosity on the acoustic impedance**

Fig. 9 represents the curve of the acoustic impedance of FPSE with porosity at different charge pressures. At a charge pressure is 2.0MPa, increasing the the porosity from 0.86 to 0.93 leads to output power and efficiency increased from 22.17W to 35.12 W and the efficiency increased from 18.44% to 23.26%. At a charge pressure is 2.5MPa, increasing the the porosity leads to output power and efficiency increased from 42.78W to 51.5W. However, the efficiency showed a tendency to increase and then decrease with the increase of porosity, and the maximum value of efficiency is 27.55% when the porosity is 0.92. At higher charge pressures, as porosity increases, the efficiency initially improves due to reduced flow resistance and enhanced mass flow. However, when porosity is beyond 0.92, the regenerator’s heat storage and exchange capability will decrease. This leads to diminished thermal regeneration effectiveness and, consequently, a decline in overall efficiency.



(a) Output power

(b) Efficiency

**Fig. 9 Effects of charge pressure and porosity on the performance**

Figures 4 to 9 illustrate that input parameters, such as regenerator’s porosity and charge pressure, have a significant impact on the output power, efficiency, and acoustic impedance of the FPSE. However, analyzing these parameters individually across a wide range of values substantially increases the computational workload. To address this challenge, we developed and employed an advanced CNN model to learn from simulation data and accurately predict the FPSE’s performance metrics. This data-driven approach not only reduces the computational cost associated with exhaustive simulations but also improves prediction accuracy and enhances the efficiency of parametric analysis. As a result, it streamlines the

optimization process and contributes to a more efficient evaluation of the FPSE's thermal-to-electric performance.

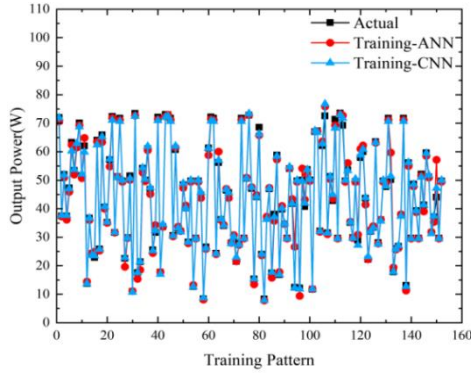
#### 4.2 CNN and ANN analysis

The output power, efficiency, and acoustic impedance of the FPSE are analyzed by varying four input parameters. The model is trained using specific parameter variations, with the prediction performance evaluated using ANN and CNN algorithms. A total of 203 datasets are generated through parameter adjustments in Sage software and numerical simulations. Typically, 70%-80% of the data are allocated for training and 30%-20% for testing. In this study, 165 datasets (approximately 80%) are used for training, while 38 datasets (approximately 20%) are reserved for testing, maintaining a training-to-testing ratio of 8:2[22]. The ANN and CNN algorithms are used to predict and analyze the actual values of output power and efficiency, and the matching relationship curves between the actual values and the predicted values are shown in Fig. 10 and Fig.11. A comparison of the evaluation metrics for the training and test sets of the two algorithms is shown in Table 1.

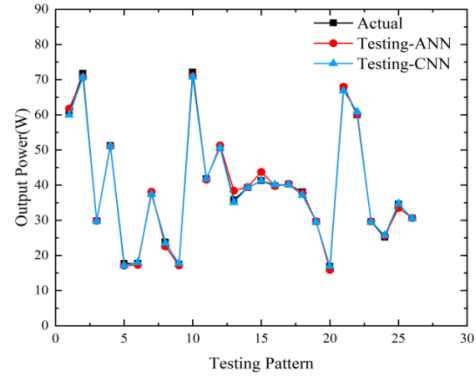
**Tab 1. Comparison of performance evaluation metrics under different algorithms**

	ANN algorithm		CNN algorithm	
	Output power	efficiency	Output power	efficiency
Training-R <sup>2</sup>	0.99577	0.99650	0.9961	0.99747
Testing-R <sup>2</sup>	0.99538	0.99330	0.99585	0.99537
Training-MSE	2.571	0.3651	1.362	0.11191
Testing -MSE	2.211	0.1469	1.3436	0.095805

As can be seen from Fig. 10 and Fig.11. The R<sup>2</sup> values obtained by the CNN algorithm for output power and efficiency in both the training and testing data are 0.99610, 0.99585, 0.99747, and 0.99537, respectively. In comparison, the R<sup>2</sup> values obtained by the ANN algorithm for output power and efficiency in the training and testing data are 0.99577, 0.99538, 0.99650, and 0.99330, with all values exceeding 0.99. However, the R<sup>2</sup> values for the CNN algorithm predictions are consistently higher than those of the ANN algorithm, indicating that the CNN algorithm provides more accurate predictions. Additionally, the MSE values obtained using the CNN algorithm are 1.3620, 1.3436, 0.11191, and 0.095805, respectively. In contrast, the MSE values for the ANN algorithm are 2.5710, 2.2111, 0.3651, and 0.1469, all of which meet the required standards. The CNN algorithm demonstrates smaller errors and more accurate predictions.

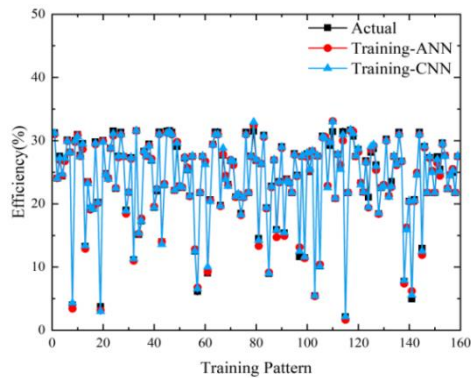


(a) Training

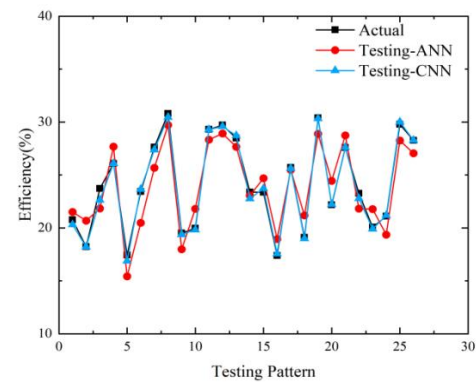


(b) Testing

**Fig. 10** Comparison of predicted and actual values of output power



(a) Training



(b) Testing

**Fig. 11** Comparison of predicted and actual values of efficiency

In summary, the ANN algorithm typically requires significant computational resources and training time, especially when applied to large-scale datasets. In contrast, the CNN algorithm offer distinct advantages by autonomously extracting hierarchical features from raw input data. This capability not only enhances the model's generalization performance but also helps reduce computational inefficiencies and potential sources of error. The CNN algorithm achieve superior predictive accuracy, characterized by narrower error margins and consistently reliable performance across test scenarios.

## 5. Conclusion

This paper establishes a thermal-dynamic coupled model of a  $\gamma$ -type FPSE based on Sage software. Through this model, the acoustic impedance and output parameters for the FPSE are analyzed in detail under different input parameters. The variations of the four different input parameters on the acoustic impedance, output power, and efficiency are investigated. In addition, the CNN and ANN are employed to predict the output performance parameters of the FPSE, and their predictive capabilities are compared. The following findings are as follows:

(1)The real part of acoustic impedance decreases and then increases with the spring stiffness of the displacer, and the minimum value of the real part of acoustic impedance is

$2.734 \times 10^7 \text{ Pa} \cdot \text{s/m}$ . When the charge pressure is 3.0MPa, the virtual part of acoustic impedance, the output power, and the efficiency all increase with the increase of spring stiffness of the displacer. These results indicate that FPSE performance is influenced by complex interactions among multiple parameters. Selecting the proper spring stiffness of the displacer springs can significantly improve the performance of FPSE.

(2) In this study, both ANN and CNN were employed to predict and analyze the selected performance parameters of the FPSE. The predictive performance of both models was evaluated using the MSE and the  $R^2$ . The results demonstrate that the CNN model achieves higher accuracy and reliability than the ANN model, especially in predicting output power and thermal-to-electric efficiency. Additionally, the CNN model consistently achieves lower MSE values than the ANN model, reflecting its enhanced generalization ability and superior capability in capturing the nonlinear relationships among design variables. These findings confirm the effectiveness of CNN-based modeling in delivering accurate and computationally efficient performance predictions, making it a valuable tool for FPSE design and optimization.

According to the comparative analysis of the results, the CNN algorithm adopted in this paper demonstrates high accuracy in predicting the parameters of the FPSE. It provides solid theoretical support for its performance design and optimization. Meanwhile, it further reveals the potential advantages of the CNN algorithm in dealing with multi-parameter interactions. Future research will prioritize experimental validation using an existing test, enabling more accurate calibration of model parameters under real-world conditions. Efforts will also be directed toward expanding the parameter to support more comprehensive performance assessments and refining the model to enhance its predictive precision. The high accuracy and broad applicability of the proposed CNN approach will be further verified through dynamic performance evaluation and real-time testing scenarios.

#### Nomenclature:

$A$	cross-sectional area, ( $\text{m}^2$ )
$d_h$	hydraulic diameter, (m)
$f$	Darcy friction factor
$F$	viscous pressure gradient, ( $\text{N} \cdot \text{m}^{-3}$ )
$I$	current, (A)
$K$	total local loss coefficient
$L$	heat exchanger length, (m)
$Nu$	nusselt number
$p$	pressure, (MPa)
$P$	pressure wave, (Pa)
$Pe$	pecelet number
$Q$	gross input heating power of system, (W)
$R$	external resistance, ( $\Omega$ )
$Re$	Reynolds number
$T$	temperature, (K)
$u$	gas velocity, ( $\text{m} \cdot \text{s}^{-1}$ )
$U$	amplitude of the volume flow rate
$W$	output power, (W)

$x$	position, (m)
$x'$	velocity, ( $\text{m} \cdot \text{s}^{-1}$ )
$x''$	accelerations, [ $\text{m} \cdot \text{s}^{-2}$ ]
$Z$	acoustic impedance, ( $\text{Pa}/(\text{m}^3/\text{s})$ )

#### Greek symbols

$\beta$	porosity
$\eta$	efficiency, (%)
$\rho$	gas density, ( $\text{kg} \cdot \text{m}^{-3}$ )

#### Subscripts

a	amplitude
b	buffer space
c	compression space
d	displacer
e	expansion
h	heater
l	cooler
p	piston
rd	displacer rod

## Acknowledgements

This paper is financially supported by the National Natural Science Foundation of China(No. 52466002), the National Natural Science Foundation of China (No. 52106027), and Hongliu Excellent Youth Talent Program Project of the Lanzhou University of Technology (2023).

## References

- [1] Chen, Y., et al., A thermally-coupled cascade free-piston Stirling engine-based cogeneration system, *Applied Thermal Engineering*, 236 (2024), 121679
- [2] Beale, W. T., Free piston Stirling engines-some model tests and simulations, *SAGE Technical Paper*, 1969
- [3] Chen, P. F., et al., Parametric investigation of the phase characteristics of a beta-type free piston Stirling engine based on a thermodynamic-dynamic coupled model, *Energy*, 20 (2022), 119658
- [4] Zare, S., et al., Design and optimization of Stirling engines using soft computing methods: a review, *Applied Energy*, 283 (2021), 116258
- [5] Li, H. Q., et al., Development of a performance analysis model for free-piston stirling power convertor in space nuclear reactor power systems, *Energies*, 15(3) (2022), 915
- [6] Zare, S., et al., Analytical investigation of free piston Stirling engines using practical stability method, *Chaos Solitons Fractals*, 167 (2023), 113082
- [7] Tavakolpour, A. R., et al., An averaging-based Lyapunov technique to design thermal oscillators: A case study on free piston Stirling engine, *Energy*, 189 (2019), 116127
- [8] Wu, Z. Y., et al., A new one-dimensional model of free-piston Stirling engine based on quasi-steady flow approximation and semi-implicit numerical method, *Applied Thermal Engineering*, 248 (2024), 123251
- [9] Ahmadi, M. H., et al., Passivity based-control technique incorporating genetic algorithm for design of a free piston Stirling engine, *Neural Computing and Applications*, 22 (2013), 1141-1150
- [10] Tavakolpour, A. R., et al., Multi-objective optimization of Stirling heat engine using gray wolf optimization algorithm, *International Journal of Engineering-Transactions C: Aspects*, 30.6 (2017), 321-329.
- [11] Chen, Z. W., et al., Load prediction of integrated energy systems for energy saving and carbon emission based on novel multi-scale fusion convolutional neural network, *Energy*, 290 (2024), 130181
- [12] Huang, S. Y., et al., Image classification and adversarial robustness analysis based on hybrid quantum-classical convolutional neural network, *Optics Communications*, 533 (2023), 129287
- [13] Kattenborn, T., et al., Review on Convolutional Neural Networks (CNN) in vegetation remote sensing, *ISPRS journal of photogrammetry and remote sensing*, 173 (2021), pp. 24-49
- [14] Gedeon, David., Sage-Object-oriented software for Stirling machine design, *In Intersociety Energy Conversion Engineering Conference*, (1994), 4106
- [15] Wang, B., et al., A high efficiency stirling-type pulse tube refrigerator for cooling above 200K, *Energy*, 215 (2021), 119120
- [16] Xu, J., et al., A thermoacoustic combined cooling, heating, and power (CCHP) system for waste heat and LNG cold energy recovery, *Energy*, 227 (2021), 120341
- [17] Luo, X. K., et al., Performance prediction and parametric optimization of  $\gamma$ -type free piston Stirling engine, *Thermal Science*, 28.1 (2024), pp. 269-281
- [18] Gedeon, D., Sage user's guide, Gedeon Associates, 2014
- [19] Dai, W., et al. Impedance match for Stirling type cryocoolers, *Cryogenics*, 51.4 (2011), pp. 168-172.
- [20] Wang, R. Y., et al., Study on the temperature adaptability of free-piston Stirling heat pump, *Energy Conversion and Management*, 249 (2021), 114864

- [21] Huang, S. Y., et al., Image classification and adversarial robustness analysis based on hybrid quantum–classical convolutional neural network, *Optics Communications*, 533 (2023), 129287
- [22] Ye, W. L., et al., Application of artificial neural network for predicting the dynamic performance of a free piston Stirling engine, *Energy*, 194 (2020), 116912

Paper submitted: 29.03.2025

Paper revised: 06.05.2025

Paper accepted: 13.05.2025